Journal of Medical Ultrasonics (2019) 46:3–14
https://doi.org/10.1007/s10396-018-0892-z

ORIGINAL ARTICLE

Ultrasound scattering by aggregated red blood cells in patients with diabetes

Hiroki Sakaki[1] · Mototaka Arakawa[1,2] · Satoshi Yashiro[3] · Yusuke Todate[3] · Yasushi Ishigaki[3] · Hiroshi Kanai[1,2]

Received: 20 March 2018 / Accepted: 5 July 2018 / Published online: 30 August 2018
© The Japan Society of Ultrasonics in Medicine 2018

Abstract

Purpose To develop methods for noninvasively and quantitatively measuring blood glucose levels.

Methods In the present study, we evaluated the degree of red blood cell (RBC) aggregation at a low shear rate robustly by introducing two new parameters determined from changes in the scattering power spectrum of the echoes from the intravascular lumen before and after cessation of blood flow. We also considered the clinical significance of these parameters and the change in sizes estimated by the conventional method by comparing them with the blood glucose level obtained just before the ultrasonic measurements. We performed the measurements in one healthy subject and 11 diabetic patients.

Results A correlation was found between one of the proposed parameters and the blood glucose level. However, the p value was not very high, and one of the reasons for the decline of the correlation will be that some factors other than blood glucose also affect RBC aggregation.

Conclusion The proposed method has potential for clinical application after elucidation of the various factors affecting RBC aggregation.

Keywords Ultrasound scattering · Red blood cells · Aggregation · Blood glucose levels

Introduction

According to the International Diabetes Federation, there were 415 million people with diabetes worldwide in 2015, i.e., 8.8% of the adult population. In Japan, diabetic patients have gradually increased up to 7.2 million people. Diabetic patients must measure their blood glucose levels with multiple skin punctures to achieve optimal blood glucose control, resulting in a burden due to the invasiveness of the procedure and the high cost of monitoring strips. Several methods for noninvasively measuring blood glucose levels have been developed, such as measurement of the heat generated during oxidation of glucose in the blood [1, 2], or measurement of light absorption by glucose [3, 4]. However, devices based on these techniques have yet to become clinically available.

On the other hand, medical ultrasound can be used repeatedly and noninvasively [5–13], and is already widely used in clinical settings. To assess the condition of a patient's blood using medical ultrasound, a great deal of research has been focused on the characteristics of backscattered echoes from red blood cells (RBCs) [14, 15]. In particular, RBC aggregation, which is a reversible adhesion phenomenon, is an important determinant of hematological properties [16, 17]. An increase in blood viscoelasticity under a constant shear rate is reported to be primarily due to an increase in RBC aggregation [18]. Moreover, blood viscosity has been confirmed to increase when blood glucose levels (BG) are high [19], leading to measurable differences, especially when the blood flow is at a low shear rate. Therefore, blood glucose levels (BG) can be assumed to be correlated with RBC aggregation. As a result, measuring RBC aggregation at low shear rates may be useful for evaluating blood glucose levels (BG).

With ultrasound imaging, though "smoke-like echoes" are known to occur in the vascular lumen based on the degree of RBC aggregation [20], this assessment is only

✉ Hiroki Sakaki
hiroshi.kanai.e7@tohoku.ac.jp

[1] Graduate School of Biomedical Engineering, Tohoku University, Sendai, Miyagi 980-8579, Japan

[2] Graduate School of Engineering, Tohoku University, Sendai, Miyagi 980-8579, Japan

[3] Department of Internal Medicine Division of Diabetes and Metabolism, Iwate Medical University, Morioka, Iwate 020-8505, Japan

qualitative. Therefore, development of a diagnostic indicator to quantitatively evaluate RBC aggregation is still needed.

Patat et al. observed changes in the speed of sound and scatterer size during the process of blood coagulation with in vitro measurements [21, 22]. Cloutier et al. estimated the size of RBC aggregation using the structure factor and attenuation estimator [23]. However, these studies were directly applied to blood collected invasively.

In our previous study, Fukushima et al. proposed a method to estimate the size of RBC aggregation by fitting the power spectrum of the scattered ultrasound wave from the intravascular lumen with theoretical scattering properties [24]. To eliminate the properties of the transfer function of the ultrasonic probe, the scattered power spectrum from the intravascular lumen was normalized by the power spectrum of the RF signal reflected from the posterior wall of the vein at the same site. Kurokawa et al. found that the effectiveness of beam selection for calculating the reflected power spectrum from the posterior wall of the vein significantly improved the accuracy of the aggregate size estimation [25]. However, the size estimation was still not stable, which can be explained by the fact that the difference in the propagation attenuation between the scattered wave from the intravascular lumen and the reflected wave from the posterior wall of the vein is not negligible.

In the present study, therefore, the degree of RBC aggregation at a low shear rate was evaluated more robustly by introducing a novel normalization method so that the difference in the propagation attenuation was removed, and new parameters were determined from changes in the scattering power spectrum of the echoes from the intravascular lumen before and after the cessation of blood flow. The present study also considered the clinical significance of the estimated size and the parameters by comparing them with the blood glucose level (BG) measured just before the ultrasonic measurements.

Materials and methods

Ultrasound backscattering

When the scattering source in a target tissue is much smaller than the wavelength of the incident wave, Rayleigh scattering occurs, and the backscattered power is proportional to the fourth power of the frequency [26, 27]. When the scatterer is much larger than the wavelength of an incident wave, reflection occurs, and the backscattered power is independent of the frequency.

In the present study, a scatterer was modeled by assuming an infinite number of infinitesimal point sources on the surface of a spherical scattering source [28]. The theoretical scattering property when the scatterer is irradiated by a plane wave is given by [29]

$$\frac{Q(ka)}{4\pi a^2} = \sum_{n=0}^{\infty} \frac{2n+1}{(ka)^2} \sin^2\left[\delta_n'(ka)\right], \tag{1}$$

where $Q(ka)$ is the scattering cross-section, k is the wave number, a is the radius of the scatterer, n is the number of point sources on the surface of the scatterer, and $\delta_n'(ka)$ is the derivative of the phase difference between the incident and scattered waves. The theoretical scattering property of each size of scatterer obtained from Eq. (1) is shown in Fig. 1. The ultrasound scattering power strongly depends on frequency. The slope of the scattering power changes by the size of the scatterer in a limited frequency range. Thus, the frequency property of the ultrasonic scattering power $|S(f)|^2$ in a certain frequency bandwidth can be approximated by

$$|S(f)|^2 = C \times f^n, \tag{2}$$

where f is the frequency, C is the coefficient, and n is the frequency dependence. The common logarithm of Eq. (2) is given by

$$\log_{10}|S(f)|^2 = n \times \log_{10} f + \log_{10} C. \tag{3}$$

The frequency dependence n shows the slope of the logarithmic power spectrum against $\log_{10} f$, and n is treated as constant in a certain frequency bandwidth, as shown in Fig. 1.

The frequency dependence n and the scattering power $|S(f)|^2$ were calculated for the theoretical scattering property in the frequency range of 27–45 MHz, as shown in Fig. 1. The results are shown in Figs. 2 and 3, respectively. As the scatterer increases in size, the frequency dependence n becomes weaker, and the scattering power increases. That is, both the frequency dependence n and the intensity of the scattering power depend on the target scatterer size. In the present study,

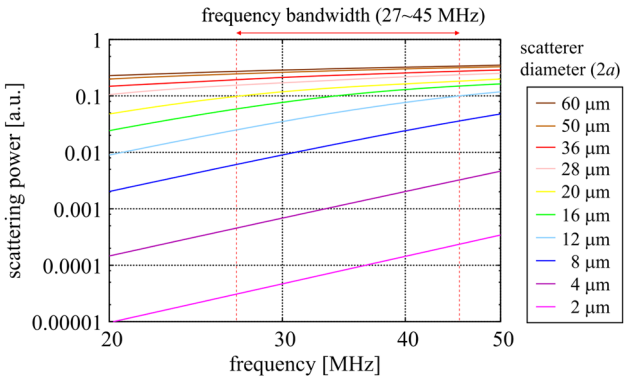

Fig. 1 Theoretical power spectrum $\log_{10}\{Q(ka)/4\pi a^2\}$ with constant values for each scatterer diameter ($2a$)

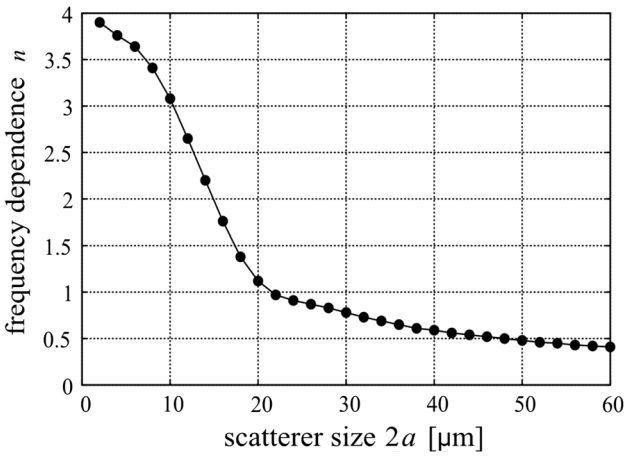

Fig. 2 Theoretical frequency dependence n for scatterer diameter ($2a$)

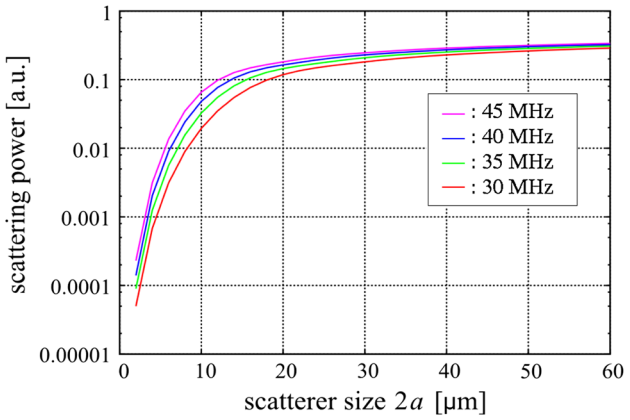

Fig. 3 Theoretical scattering power for scatterer diameter ($2a$)

40-MHz ultrasonic waves (wavelength = 38.5 μm) were used to target a wide range of particle sizes, from a single RBC (maximum width = 8 μm) to large RBC aggregates. From Figs. 1, 2, 3, the amplitude changes are larger for smaller scatterers at 27–45 MHz. Therefore, the sensitivity of size estimation for the larger scatterers should be less than that for the smaller scatterers.

However, the ultrasonic scattering power spectrum $P_s(f,d)$ of the measured signal calculated by Eq. (4) includes four frequency properties other than the scattering property $S(f)$ exhibiting a frequency dependence particular to the scatterer size, as follows:

$$P_s(f,d) = |S(f)A(f,d)H(f,d)G(f)X(f)|^2, \tag{4}$$

where d is the depth, $X(f)$ is the frequency spectrum of the input voltage applied to the transducer, $G(f)$ is the frequency response of the transmitting and receiving properties of the transducer, $H(f,d)$ is the sound pressure property for focus formation, and $A(f,d)$ is the attenuation property of the propagation medium. $X(f)$ and $G(f)$ depends on the ultrasonic probe and the ultrasonic equipment, and $H(f,d)$ depends on the positions irradiated by the ultrasonic probe. These three components can be assumed to be constant when the ultrasonic probe is kept in the same position over the course of the measurements. Therefore, they can be removed by normalizing the power spectrum acquired under the same measurement conditions.

Extracting the scattering property by normalization

In the previous methods in our group [24, 25], $P_S(f,d)$ was normalized by the reflected power spectrum $P_r(f,d)$ from the posterior wall of the vein to extract the scattering property $|S(f)|^2$. This process is expressed by

$$10\log_{10}\frac{P_s(f,d_0)}{P_r(f,d_0)} = 10\log_{10}\frac{\left|S(f)A_s(f,d_0)H(f,d_0)G(f)X(f)\right|^2}{\left|R(f)A_r(f,d_0)H(f,d_0)G(f)X(f)\right|^2}$$

$$\approx 10\log_{10}\frac{|S(f)|^2}{|R_0|^2}, \tag{5}$$

where d_0 is the focal length of the ultrasonic probes, the amplitude spectra $A_s(f,d_0)$ and $A_r(f,d_0)$ are the attenuation properties in the measurements of $P_s(f,d_0)$ and $P_r(f,d_0)$, respectively, and $|R(f)|^2$ is the reflection property from the wall of the vein. Assuming that $R(f)$ is independent of the frequency ($n = 0$), it was approximated to be constant R_0.

Figure 4a, b show the schematic diagram of acquisition of RF signals scattered from RBCs to obtain the scattered power spectrum $P_s(f,d_0)$ and that of RF signals reflected from a flat posterior wall of the vein to obtain the reflected power spectrum $P_r(f,d_0)$, respectively, in the previously proposed method. By considering the three attenuation properties—the attenuation property $A_w(f,d)$ in water and ultrasonic echo gel, the attenuation property $A_t(f,d)$ in hypodermal tissues, and the attenuation property $A_b(f,d)$ in blood—each of the attenuation properties $A_s(f,d_0)$ and $A_r(f,d_0)$ in $P_s(f,d_0)$ and $P_r(f,d_0)$ of Eq. (5) can be divided into the three components as follows:

$$\log_{10}A_s(f,d_0) = \log_{10}A_w(f,d_1) + \log_{10}A_t(f,d_2) + \log_{10}A_b(f,d_3), \tag{6}$$

$$\log_{10}A_r(f,d_0) = \log_{10}A_w(f,d_1-d_3) + \log_{10}A_t(f,d_2) + \log_{10}A_b(f,2d_3), \tag{7}$$

where d_1, d_2, and d_3 are the propagation distances in water, hypodermal tissue, and blood, respectively, as shown in Fig. 4, and both equations satisfy the relationship

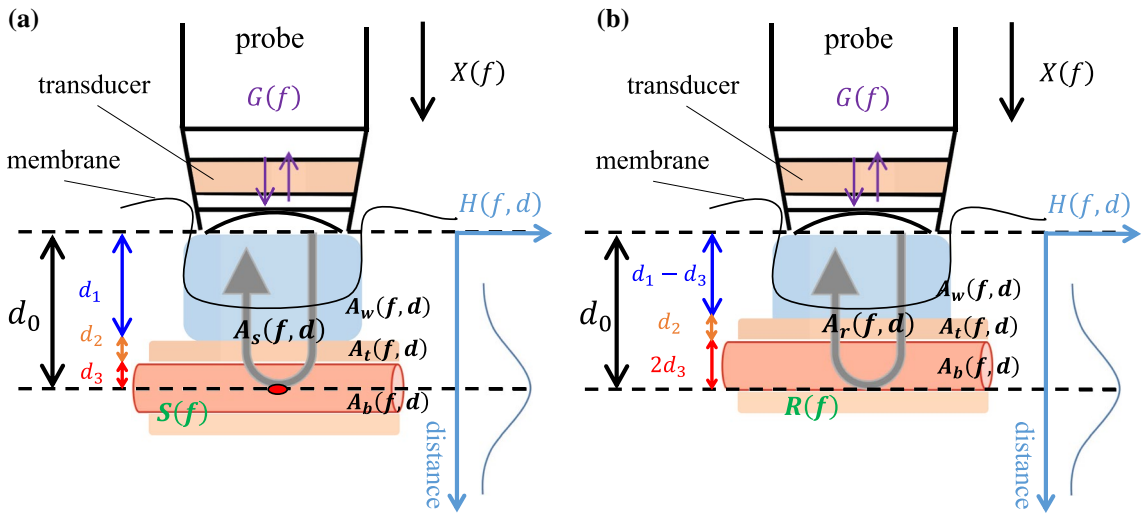

Fig. 4 Schematic diagrams of acquisitions of RF signals from **a** RBCs and **b** a flat posterior wall of the vein

$d_0 = d_1 + d_2 + d_3$. The difference in the propagation distances in water and blood in Eqs. (6) and (7) comes from setting of the different targets at the center of the intravascular lumen or the posterior wall of the vein, respectively, at the focal length d_0. In the approximation $A_s(f, d_0) \approx A_r(f, d_0)$ applied in Eq. (5), the following difference $10\log_{10}\left|\Delta A(f, d_0)\right|^2$ in those attenuation properties remains as an error in the strict sense as follows:

$$
\begin{aligned}
&10\log_{10}\left|\Delta A(f, d_0)\right|^2 \\
&= 10\log_{10}\left|A_s(f, d_0)\right|^2 - 10\log_{10}\left|A_r(f, d_0)\right|^2 \\
&= 20\{\log_{10}A_w(f, d_1) + \log_{10}A_b(f, d_3) \\
&\quad - \log_{10}A_w(f, d_1 - d_3) - \log_{10}A_b(f, 2d_3)\} \\
&= 20\{\log_{10}A_w(f, d_3) + \log_{10}A_b(f, -d_3)\}. \qquad (8)
\end{aligned}
$$

By introducing $10\log_{10}\left|\Delta A(f, d_0)\right|^2$, Eq. (5) can be rewritten without approximation as follows:

$$
10\log_{10}\frac{P_s(f, d_0)}{P_r(f, d_0)} = 10\log_{10}\frac{|S(f)|^2}{|R_0|^2} + 10\log_{10}\left|\Delta A(f, d_0)\right|^2. \qquad (9)
$$

Since the attenuation coefficient of water is $\alpha_w/f^2 = 24.4 \times 10^{-18}\ \mathrm{s}^2/\mathrm{mm}$ [30], the attenuation coefficient of blood is $\alpha_b/f^{1.14} = 36.6 \times 10^{-11}\ \mathrm{s}^{1.14}/\mathrm{mm}$ [31], and d_3 is 1.0 mm based on past experiments in our group, $10\log_{10}\left|\Delta A(f, d_0)\right|^2$ of Eq. (8) can be approximated by

$$
\begin{aligned}
10\log_{10}\left|\Delta A(f, d_0)\right|^2 \approx &- 423.9 \times 10^{-18} \times f^2 + 635.8 \\
&\times 10^{-11} \times f^{1.14}\ (\mathrm{dB}), \qquad (10)
\end{aligned}
$$

where $A_w(f, d) = e^{-\alpha_w \times 2d}$ and $A_b(f, d) = e^{-\alpha_b \times 2d}$ were assumed.

Figure 5 shows the frequency characteristics of $10\log_{10}\left|\Delta A(f, d_0)\right|^2$ of Eq. (10). Since the reflection property $|R_0|^2$ was assumed to be a constant as in Eq. (5) in the previous method, the slope n of the normalized power spectrum $10\log_{10}\{P_s(f, d_0)/P_r(f, d_0)\}$ for $\log_{10}f$ was fitted to the theoretical scattering property. However, as shown in Fig. 5, since the difference $10\log_{10}\left|\Delta A(f, d_0)\right|^2$

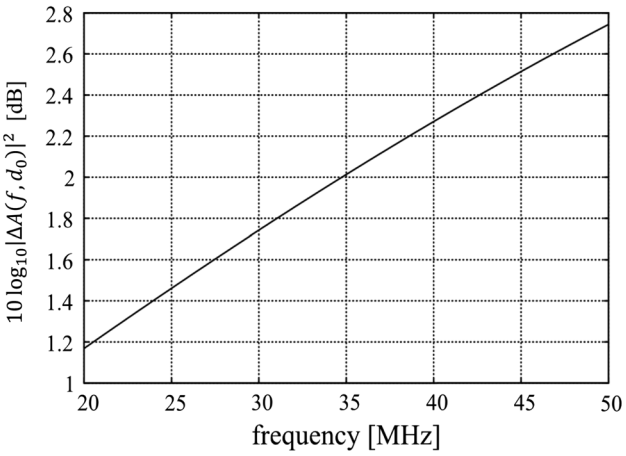

Fig. 5 Frequency properties of $10\log_{10}\left|\Delta A(f, d_0)\right|^2$

still exhibits frequency dependence, a systematic error occurs in the determination of the slope n of the power spectrum $10\log_{10}\{P_s(f,d_0)/P_r(f,d_0)\}$ in Eq. (5), which introduces an error in the estimated size.

To suppress the systematic error due to the path length difference, the present study proposes a new method for normalization using the scattered power spectra of two different scatterer sizes as follows. Figure 6 shows the schematic view of acquisitions of RF signals scattered from two different scatterers. The smaller scatterers in Fig. 6a and larger scatterers in Fig. 6b correspond to RBCs before aggregation and RBC aggregates, respectively. The two different scattering power spectra can be obtained by acquiring RF signals scattered from RBCs before and after the stop of the blood flow, which suppresses the effect due to the difference in path length that occurred in the previous method, and the propagation attenuation $A(f,d)$ can be removed by the following normalization.

$$10\log_{10}\frac{P_{s_{\mathrm{ava}}}(f,d_0)}{P_{s_{\mathrm{rest}}}(f,d_0)} = 10\log_{10}\frac{\left|S_{\mathrm{ava}}(f)A_s(f,d_0)H(f,d_0)G(f)X(f)\right|^2}{\left|S_{\mathrm{rest}}(f)A_s(f,d_0)H(f,d_0)G(f)X(f)\right|^2}$$

$$= 10\log_{10}\frac{\left|S_{\mathrm{ava}}(f)\right|^2}{\left|S_{\mathrm{rest}}(f)\right|^2}, \tag{11}$$

where $P_{s_{\mathrm{rest}}}(f,d_0)$ is the scattered power spectrum from the smaller scatterer, $P_{s_{\mathrm{ava}}}(f,d_0)$ is that from the larger scatterer, $S_{\mathrm{rest}}(f)$ is the spectrum of scattering property of the smaller scatterer at rest, and $S_{\mathrm{ava}}(f)$ is that of the larger scatterer after avascularization. Normalization in Eq. (11) extracts the change in the scattering properties for two scatterer sizes as $10\log_{10}\left\{\left|S_{\mathrm{ava}}(f)\right|^2\Big/\left|S_{\mathrm{rest}}(f)\right|^2\right\}$.

From Eq. (2), the scattering properties $\left|S_{\mathrm{rest}}(f)\right|^2$ and $\left|S_{\mathrm{ava}}(f)\right|^2$ can be expressed as

$$\left|S_{\mathrm{rest}}(f)\right|^2 = C_{\mathrm{rest}}\times f^{n_{\mathrm{rest}}},$$

$$\left|S_{\mathrm{ava}}(f)\right|^2 = C_{\mathrm{ava}}\times f^{n_{\mathrm{ava}}},$$

where C_{rest} and C_{ava} are coefficients, and n_{rest} and n_{ava} are the frequency dependences for the smaller scatterer and the larger scatterer, respectively. As shown in Fig. 1, these four coefficients can be assumed to be constant in a certain frequency bandwidth.

The normalized power spectrum $P_{s_{\mathrm{norm}}}(f,d_0)$ is defined by the ratio of the scattering power of the larger scatterer to that of the smaller scatterer as follows:

$$P_{s_{\mathrm{norm}}}(f,d_0) = \frac{\left|S_{\mathrm{ava}}(f)\right|^2}{\left|S_{\mathrm{rest}}(f)\right|^2}$$

$$= \frac{C_{\mathrm{ava}}}{C_{\mathrm{rest}}}\times f^{n_{\mathrm{ava}}-n_{\mathrm{rest}}}, \tag{12}$$

where the frequency dependence in $P_{s_{\mathrm{norm}}}(f,d_0)$ expresses the change $n_{\mathrm{ava}}-n_{\mathrm{rest}}$ in the frequency dependence of the larger scatterer from that of the smaller scatterer.

We introduce the following two new parameters, ρ and Δn, for evaluation of the scattering power ratio

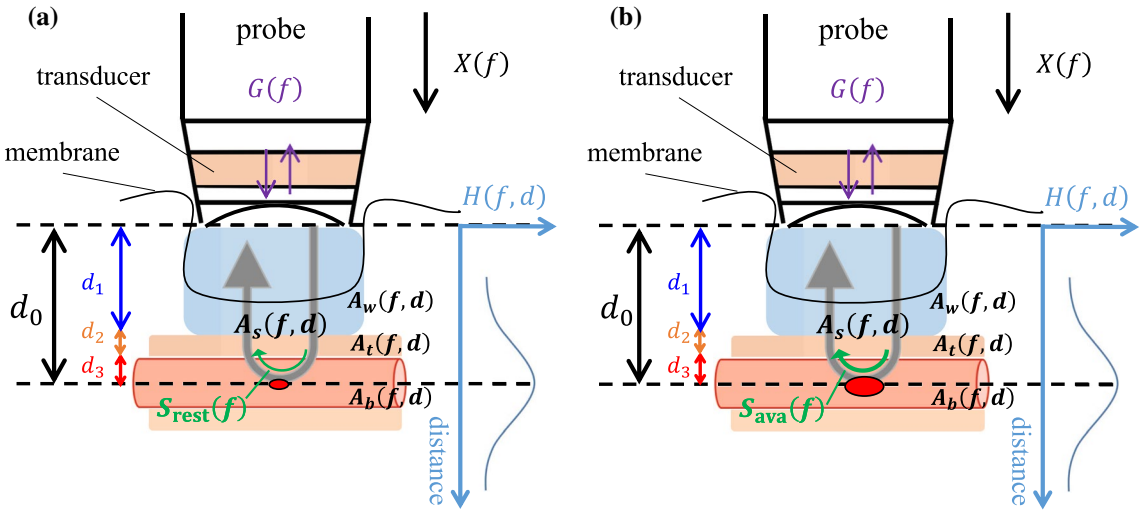

$$P_{s\mathrm{rest}}(f,d_0) = \left|S_{\mathrm{rest}}(f)A_s(f,d_0)H(f,d_0)G(f)X(f)\right|^2$$

$$P_{s\mathrm{ava}}(f,d_0) = \left|S_{\mathrm{ava}}(f)A_s(f,d_0)H(f,d_0)G(f)X(f)\right|^2$$

Fig. 6 Schematic diagrams of acquisitions of RF signals from the **a** smaller and **b** larger scatterers

$|S_{\mathrm{ava}}(f)|^2 \Big/ |S_{\mathrm{rest}}(f)|^2$ and the change $n_{\mathrm{ava}} - n_{\mathrm{rest}}$ in the frequency dependences, respectively. First, the parameter ρ concerned with the scattering power ratio is expressed by

$$\rho = \underset{f_1 \le f \le f_2}{E} \left[10 \log_{10} P_{s_{\mathrm{norm}}}(f, d_0) \right], \tag{13}$$

where f_1 and f_2 were determined by considering the bandwidth of the ultrasonic probe. From Eq. (13), the scattering power ratio ρ is calculated by averaging the power of the normalized power spectrum within the bandwidth.

Next, the parameter Δn concerned with the change in the frequency dependences is expressed by

$$\Delta n = n_{\mathrm{ava}} - n_{\mathrm{rest}}, \tag{14}$$

which shows the slope of the logarithmic normalized power spectrum within the probe bandwidth in the following equation:

$$\log_{10} P_{s_{\mathrm{norm}}}(f, d_0) = \Delta n \times \log_{10} f + \log_{10} \left(\frac{C_{\mathrm{ava}}}{C_{\mathrm{rest}}} \right), \tag{15}$$

where the frequency bandwidth in the present study was set at 27–45 MHz.

Figure 7 shows $10 \log_{10} P_{s_{\mathrm{norm}}}(f, d_0)$ calculated using Eq. (12), when the sizes of the smaller and larger scatterers are 5 and 20 μm, respectively, where the theoretical scattering property for each scatterer was calculated by Eq. (1). The average of the normalized power corresponds to ρ, and 1/10 of the slope of the normalized power spectrum corresponds to Δn. As shown in Fig. 7, Δn can be assumed to be almost constant in the bandwidth (27–45 MHz).

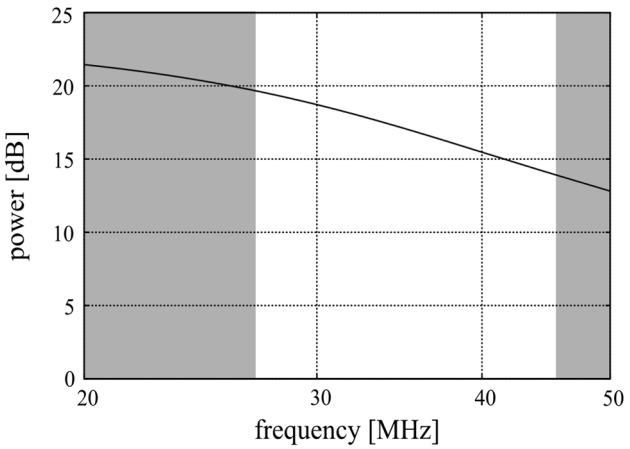

Fig. 7 $10 \log_{10} P_{s_{\mathrm{norm}}}(f, d_0)$ in the case that sizes of the smaller and larger scatterers are 5 and 20 μm

Basic experiments using microspheres

Ultrasonic diagnostic equipment (UD-8000; Tomey, Japan) with a mechanical scan probe operating at the central frequency of 40 MHz and a focal length of 9 mm was used. The number of beams was 113. The beams were in the same direction, and B-mode images were obtained from all the beams. The RF echoes were acquired at a sampling frequency of 240 MHz, and their power spectra were obtained by applying the Fourier transform with a Hanning window of 0.15 μs at three positions along the depth direction for each beam. The central window was set to the beam focal depth, and the remaining windows were set to the depth shifted up or down by 0.075 μs from the focal depth. The mean scattered power spectrum for each frame was obtained by averaging the power spectra of 339 signals detected from all 113 beams.

Microspheres (Polyamide Seeding Particles; Dantec Dynamics, Denmark) with diameters of 5 and 20 μm were used for simulating RBCs before aggregation and RBC aggregates, respectively. The size distributions were 1–10 μm for 5-μm particles and 5–35 μm for 20-μm particles. The shape was not spherical but round. The number density was 6×10^3 and 9×10^1 mm^{-3} for 5- and 20-μm particles, respectively. The single RBC has a diameter of 8 μm. The concentration of the aqueous solution of the microspheres was 3.0 g/l. Before and after RBC aggregation, there should be no change in the weight concentration of the RBCs. Therefore, we made the weight concentration of microspheres for 5-μm and that of 20-μm particles the same in the experiment. Each aqueous solution containing microspheres with different diameters was prepared in a beaker. The surface of the ultrasonic probe was inserted into the solution in a stationary state. To disperse the microspheres, polyoxyethylene octylphenyl ether was used as the surfactant.

Nineteen frames of RF echoes were acquired every 5 s. To maintain the measurement conditions, the Hanning window was set at the same depth during the acquisition of the 19 frames. The scattering power ratio ρ and the change in the frequency dependences Δn were calculated from $P_{s_{\mathrm{rest}}}(f, d_0)$ and $P_{s_{\mathrm{ava}}}(f, d_0)$, which were obtained by averaging the power spectra of the 19 frames during the measurement for the microspheres of 5 and 20 μm, respectively.

In vivo experiments

We performed in vivo experiments on human dorsal hand veins. RBC aggregation tends to occur when the blood shear rate becomes low [32]. Therefore, we measured ultrasonic echoes from RBCs with and without blood flow. The blood flow was almost stopped using the application of about 250 mmHg

of pressure using a cuff on the upper arm, and the condition was confirmed on the B-mode image.

The measurement procedure was as follows. First, the posterior wall of the vein was set as the focus of the ultrasonic probe, and RF echoes from the lumen-intima interface were acquired. Then, the reflected power spectrum $P_r(f, d_0)$ of Eq. (5) was calculated from the acquired RF echoes, and it was used for normalization by the previous method. Then, the lumen of the vein was set as the focus, and the RF echoes from the RBCs were acquired while the subject was at rest for 1 min and under avascularization conditions for 2 min. A total of 19 frames of RF echoes were acquired every 10 s. The power spectrum of the smaller scatterer, $P_{s_{\text{rest}}}(f, d_0)$, was obtained by averaging the power spectra of the first seven frames at rest. The power spectrum of the larger scatterer, $P_{s_{\text{ava}}}(f, d_0)$, was obtained by averaging the power spectra of the six frames acquired during the latter half of the avascularization period. Therefore, the scattering power ratio ρ of Eq. (13) and the change in the frequency dependences Δn of Eq. (14) were obtained.

As a comparison, each scatterer size $2a$ was estimated based on the previously developed method [25] from the scattered averaged power spectra $\{P_s(f, d_0)\}$ obtained for the rest and avascularization phases. Then, the increase $\Delta(2a)$ in the average estimated size from the rest phase to the avascularization phase was estimated.

Ultrasonic measurements were repeatedly performed in one healthy subject under various conditions, including the fasting or post-prandial state. Then, the three parameters ρ, Δn, and $\Delta(2a)$ described above were obtained. Just before each ultrasonic measurement, the blood glucose level (BG) was measured using a blood glucose measuring device (FreeStyle Freedom Lite®; NIPRO, Japan). The fact that the subject was healthy was judged based on not satisfying Diabetes Evaluation Criteria reported by the World Health Organization in 2006 [33].

Ultrasonic measurements were also performed in 11 diabetic patients. For each analyzed subject, the plasma layer was observed in the uppermost intravascular lumen during the latter half of the avascularization period. This plasma layer is thought to form as a result of the RBC aggregation in the central region of the lumen, which depletes the concentration in the uppermost intravascular lumen. The blood glucose levels (BG) were examined just before the ultrasonic measurement.

We compared the parameters ρ, Δn, and $\Delta(2a)$ with the blood glucose level (BG) for each measurement. The value of the correlation was evaluated by the coefficient of determination R^2 of the straight-line fit, defined by

$$R^2 \equiv 1 - \frac{\sum_i \left(y_i - f(x_i)\right)^2}{\sum_i \left(y_i - \bar{y}\right)^2}, \tag{16}$$

where y_i is measurement data, $f(x_i)$ is a linear regression model, and $\bar{y}$ is the averaged value of y_i.

Results and discussion

Basic experiments using microspheres

Theoretical values of the scattering power ratio ρ and the change in the frequency dependences Δn for the sizes of 5 and 20 μm were calculated as 16.7 dB and −2.60, respectively, from Fig. 1. On the other hand, those were measured for microspheres of 5 and 20 μm as 16.9 dB and −2.30, respectively. While ρ almost corresponded to the theoretical value, Δn was slightly different from the theoretical one. The robustness of each parameter against the influence of noise was considered as follows.

The acquired RF signals include noise components other than the signal components. By introducing the frequency property $N_s(f)$ of noise components, the scattered power spectrum of Eq. (4) can be replaced by $P_{s+N}(f, d)$ including noise components as

$$P_{s+N}(f, d) = \left|S(f)A(f, d)H(f, d)G(f)X(f) + N_s(f)\right|^2. \tag{17}$$

By assuming that there is no correlation between the signal component and noise components,

$$P_{s+N}(f, d) = P_s(f, d) + P_N(f), \tag{18}$$

where $P_N(f)$ is the power spectrum of noise components.

Figure 8 compares the experimental spectrum $10\log_{10} P_{s_{\text{norm}}}(f, d_0)$(dB) from the theoretical one calculated from Eq. (1). The scattering power ratio ρ can be obtained by averaging $10\log_{10} P_{s_{\text{norm}}}(f, d_0)$ in the bandwidth. Figure 9

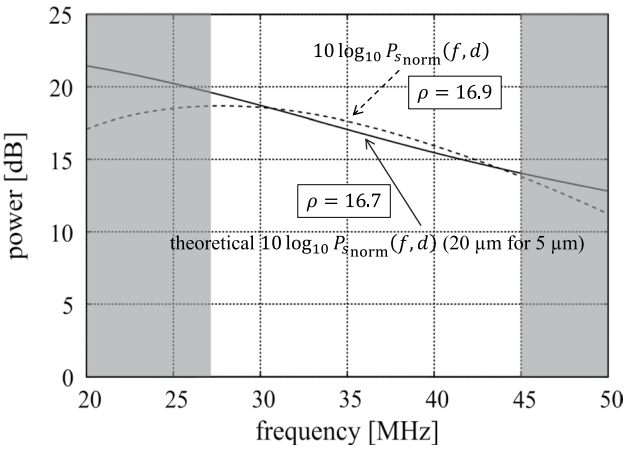

Fig. 8 Comparison between the experimental $10\log_{10} P_{s_{\text{norm}}}(f, d_0)$ and the theoretical one

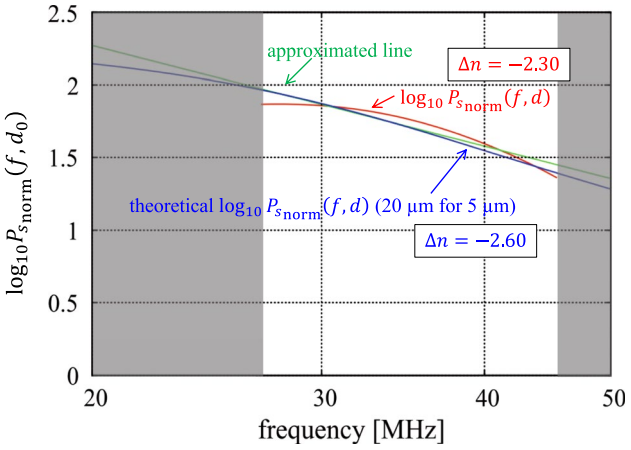

Fig. 9 Comparison between the experimental $\log_{10} P_{s_{\mathrm{norm}}}(f, d_0)$ and the theoretical one, and the approximate theoretical straight line for calculating Δn

compares the experimental spectrum $\log_{10} P_{s_{\mathrm{norm}}}(f, d_0)$ from the theoretical one calculated from Eq. (1), and the straight line for calculating Δn is shown.

As shown in Figs. 8 and 9, at the frequency close to the outside of the frequency bandwidth (especially around 27 MHz), the power of the experimental spectrum $10\log_{10} P_{s_{\mathrm{norm}}}(f, d_0)$ was lower than the theoretical value. By assuming that the power of the experimental spectrum includes noise components $P_N(f)$ and they are constant as P_N, it is expressed by

$$
\begin{aligned}
&10\log_{10} P_{s_{\mathrm{norm}+N}}(f, d_0) \\
&= 10\log_{10} \frac{P_{s_{\mathrm{ava}}}(f, d_0) + P_N}{P_{s_{\mathrm{rest}}}(f, d_0) + P_N} \\
&= 10\log_{10} \left\{ P_{s_{\mathrm{ava}}}(f, d_0) \left(1 + \frac{P_N}{P_{s_{\mathrm{ava}}}(f, d_0)} \right) \right\} \\
&\quad - 10\log_{10} \left\{ P_{s_{\mathrm{rest}}}(f, d_0) \left(1 + \frac{P_N}{P_{s_{\mathrm{rest}}}(f, d_0)} \right) \right\} \\
&= 10\log_{10} P_{s_{\mathrm{norm}}}(f, d_0) + 10 \left\{ \log_{10} \left(1 + \frac{P_N}{P_{s_{\mathrm{ava}}}(f, d_0)} \right) \right. \\
&\quad \left. - \log_{10} \left(1 + \frac{P_N}{P_{s_{\mathrm{rest}}}(f, d_0)} \right) \right\}. \qquad (19)
\end{aligned}
$$

Thus, the experimental value including the noise component has the additive power difference of $10\{\log_{10}(1 + P_N/P_{s_{\mathrm{ava}}}(f, d_0)) - \log_{10}(1 + P_N/P_{s_{\mathrm{rest}}}(f, d_0))\}$ compared with the theoretical value without noise components. Therefore, the degree of such influence is roughly dominated by the ratio of P_N to $P_{s_{\mathrm{ava}}}(f, d_0)$ and $P_{s_{\mathrm{rest}}}(f, d_0)$. On the other hand, when $P_{s_{\mathrm{ava}}}(f, d_0)$ and $P_{s_{\mathrm{rest}}}(f, d_0)$ are sufficiently larger than P_N, the influence of noise components is negligible. However, as shown in Fig. 3, the scattering power $P_{s_{\mathrm{rest}}}(f, d_0)$ of the smaller scatterer is smaller than $P_{s_{\mathrm{ava}}}(f, d_0)$ of the larger scatterer, especially at a lower frequency. Furthermore, −6 dB bandwidth in the experiment in the present study was 27–45 MHz. Therefore, $P_{s_{\mathrm{rest}}}(f, d_0)$ around 27 MHz is assumed to be small, and the influence of the noise of the last term of Eq. (19) cannot be canceled, and then the normalized power of Eq. (19) decreases from $10\log_{10} P_{s_{\mathrm{norm}}}(f, d_0)$ of Eq. (11), which introduces error in the estimation of the parameters of ρ and Δn.

As shown in Fig. 8, since the scattering power ratio ρ was calculated by averaging the normalized power within the frequency bandwidth, errors generated around 27 MHz can be reduced. On the other hand, since the change in the frequency dependences Δn was calculated by approximating the slope of the normalized power within the frequency bandwidth as shown in Fig. 9, Δn was unfortunately affected by errors around 27 MHz. Therefore, the scattering power ratio ρ is more robust than Δn.

In vivo measurements

The parameters ρ, Δn, and $\Delta(2a)$ were compared with the blood glucose level (BG) for each measurement in one healthy subject under various conditions, including the fasting or post-prandial state, as shown in Fig. 10. A blood glucose level higher than 100 mg/dl corresponds to the data measured after meals. From Fig. 10a, the highest correlation was obtained for the relationship between the ratio ρ and (BG).

Next, for 11 diabetic patients, the parameters ρ, Δn, and $\Delta(2a)$ were compared with the blood glucose level (BG), as shown in Fig. 11. From Fig. 11a, the highest correlation was also found between the ratio ρ and (BG).

The p value of the scattering power ratio ρ and the blood glucose level was 0.03 ($* p < 0.05$) for the healthy subject, and that for the diabetic patients was 0.19 ($p > 0.05$). Thus, clinical significance was somewhat shown in the one healthy subject and not shown in the diabetic patients.

Therefore, the following additional experiments were performed in the same healthy subject three times, which we refer to as Ex. A, B, and C. In each experiment, the ultrasonic measurements and blood glucose level (BG) measurements were performed after fasting for 12 h. Both measurements were performed five times at intervals of about 30 min. Table 1 shows the blood glucose level (BG) and the scattering power ratio ρ for each experiment as a function

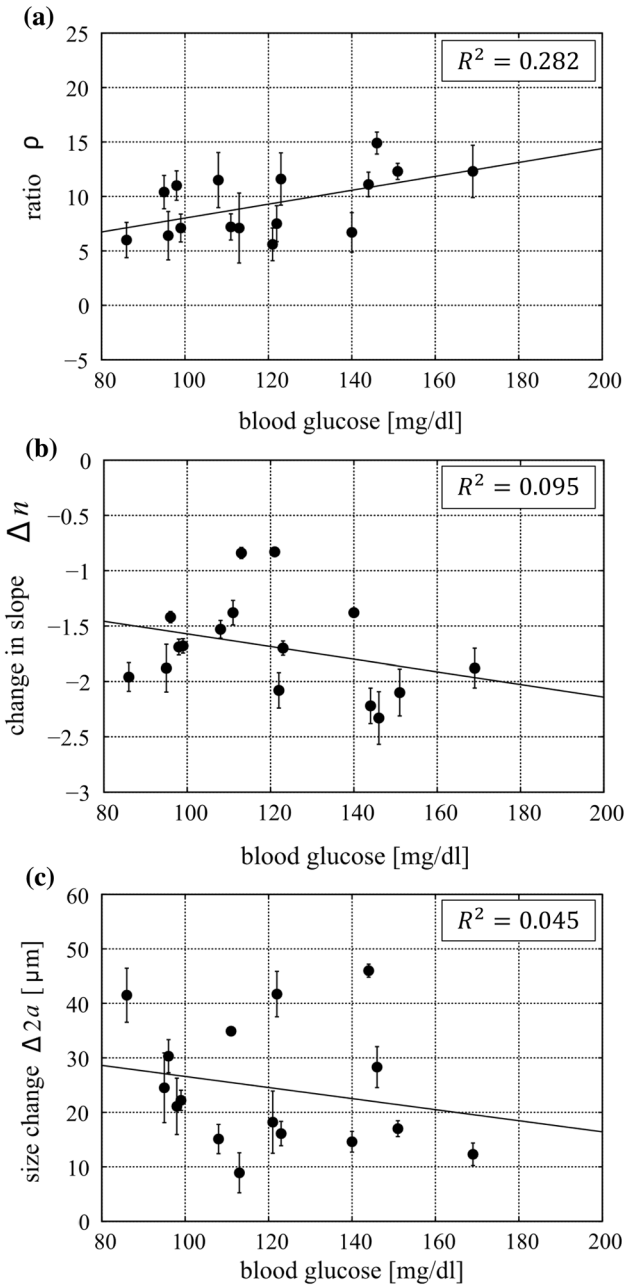

Fig. 10 The blood glucose level and three analysis parameters, which are **a** ρ, **b** Δn, and **c** $\Delta(2a)$, in a healthy subject. Closed circles: measurement data, solid line: approximated line

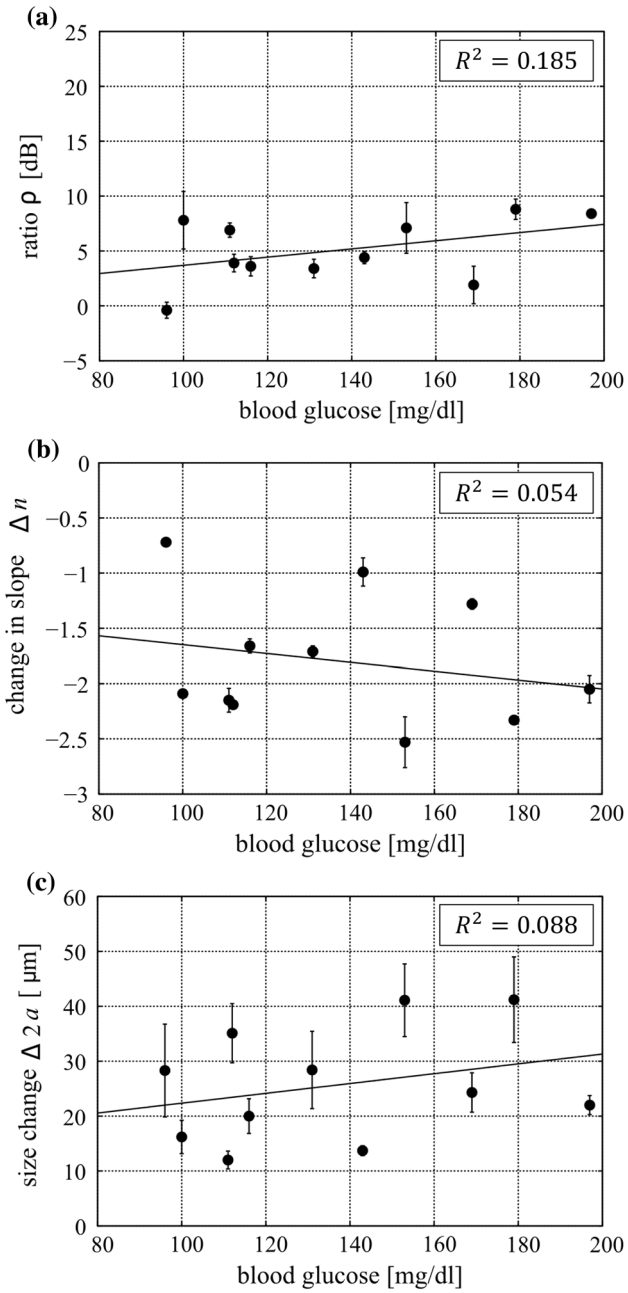

Fig. 11 The blood glucose level and three analysis parameters, which are **a** ρ, **b** Δn, and **c** $\Delta(2a)$, in 11 diabetic patients. Closed circles: measurement data, solid line: approximated line

of time from the ingestion of glucose. Glucose (18 g) was ingested just before the second measurement in Ex. A, and just before the third measurement in Ex. B and C. With the exception of Ex. C, both the blood glucose level (BG) and the scattering power ratio ρ remarkedly increased just after ingestion of glucose. On the other hand, the blood glucose level (BG) further increased despite the scattering power ratio ρ decreasing 30 min after ingestion of glucose.

We discuss this transition as follows: Fig. 12 shows the power of $10\log_{10} P_{s_{\text{rest}}}(f, d_0)$ and $10\log_{10} P_{s_{\text{ava}}}(f, d_0)$ of Eq. (11) against the time from ingestion of glucose in each experiment. From Fig. 12, for all experiments, the power of $10\log_{10} P_{s_{\text{rest}}}(f, d_0)$ decreased immediately after ingestion of glucose.

Figure 13a, b show the B-mode image during the resting period in measurements 2 and 3, respectively, in Ex. B. The brightness in the intravascular lumen became clearly low

Table 1 Blood glucose level and scattering power ratio ρ of each experiment as a function of time from ingestion of glucose

In vivo measurement times	Time from ingestion of glucose (min)	Blood glucose (mg/dl)	Scattering power ratio ρ (dB)
Experiment A			
1	−35	93	5.6
2	+5	119	11.4
3	+33	160	8.5
4	+77	85	8.6
Experiment B			
1	−35	93	9.1
2	−27	93	6.4
3	+10	122	12.9
4	+34	142	10.3
5	+68	76	9.7
Experiment C			
1	−79	89	10.6
2	−37	89	8.6
3	+14	137	7.7
4	+39	124	4.8
5	+67	77	0.8

in measurement 3 as compared with measurement 2. Thus, RBCs did not aggregate in the rest period after ingestion of glucose. Although the cause is unknown, some factors other than the blood glucose level (BG) also influenced the aggregation of RBCs. Thus, the correlation between the scattering power ratio ρ and the blood glucose level (BG) decreased. We will continue to investigate the factors.

Conclusion

The present study proposed a new normalization method for avoiding the effect of path length difference to accurately evaluate the degree of RBC aggregation by introducing new parameters ρ and Δn. The ultrasound-based method proposed in the present study is noninvasive and inexpensive compared with other instruments for measuring blood glucose levels (BG). There is a possibility that some factors other than blood glucose affected the RBC aggregation, and a few problems with the proposed method still remain, but the method has the potential to noninvasively measure blood glucose levels (BG). In the proposed method, it is necessary to perform measurements during flow and under stationary conditions. However, the Doppler effect does not affect the measurement, because of the difference in the ultrasonic velocity in blood and blood flow velocity. Otherwise, the difference in propagation loss caused by the different scattering under the different

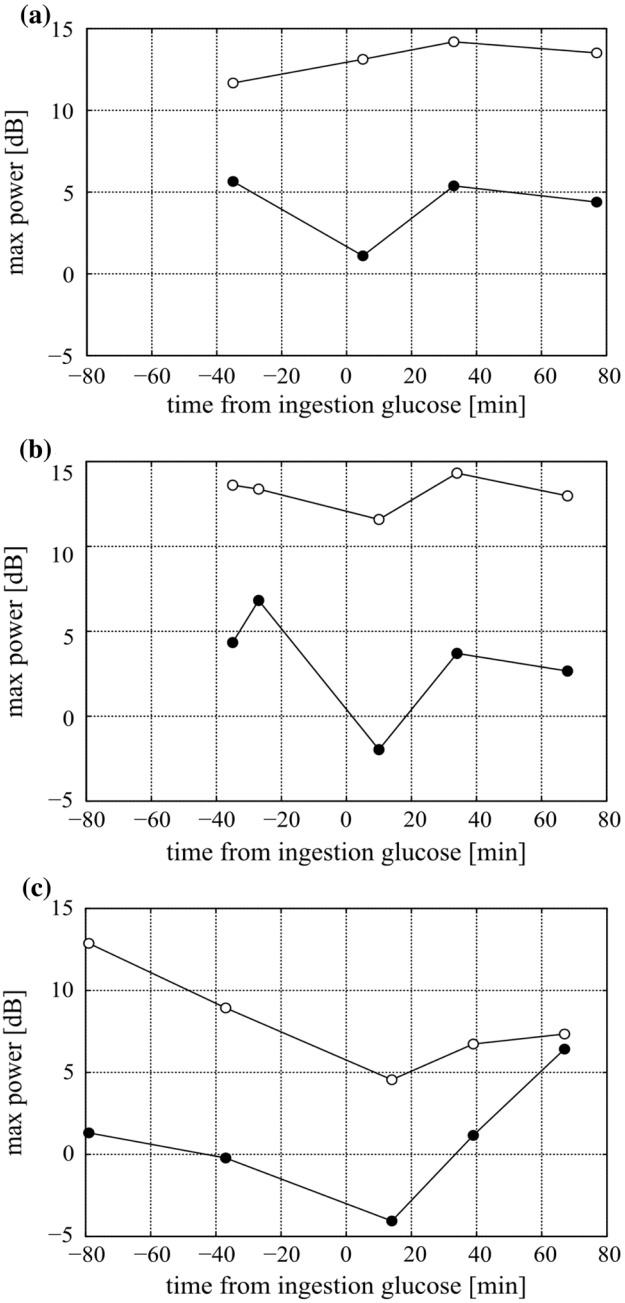

Fig. 12 The maximum power of $10\log_{10} P_{s_{\text{rest}}}(f, d_0)$ (solid circles) and $10\log_{10} P_{s_{\text{ava}}}(f, d_0)$ (open circles) against the time from ingestion of glucose in Experiments **a** A, **b** B, and **c** C

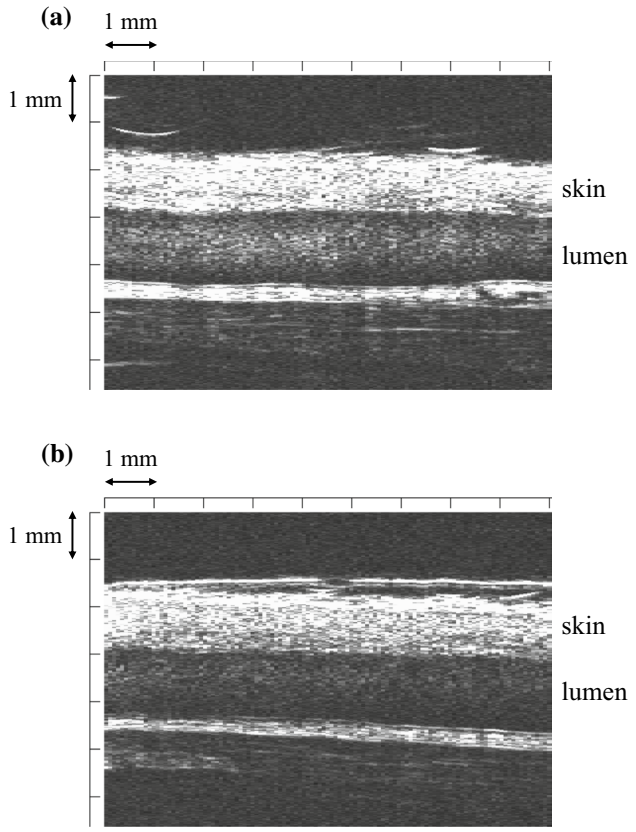

Fig. 13 B-mode image of the resting period in **a** measurement 2 and **b** measurement 3

conditions would affect the measurement. We will discuss this effect in a future paper.

Acknowledgements This work was partly supported by MEXT/JSPS KAKENHI through Grant No. 16K14272.

Compliance with ethical standards

This study was approved by the Institutional Review Board of Iwate Medical University (Approval Number: H26-79). Written informed consent was obtained from study participants.

Conflict of interest The authors have no conflicts of interest with regard to the presented research.

References

1. Cho O, Kim Y, Mitsumaki H, et al. Noninvasive measurement of glucose by metabolic heat conformation method. Clin Chem. 2004;50:1894–8.
2. Zhang Y, Zhu J, Liang Y, et al. Non-invasive blood glucose detection system based on conservation of energy method. Physiol Meas. 2017;38:325–42.
3. Kinnunen M, Myllylä R. Effect of glucose on photoacoustic signals at the wavelengths of 1064 and 532 nm in pig blood and intralipid. J Phys D Appl Phys. 2005;38:2654–61.
4. Lan YT, Kuang YP, Zhou LP, et al. Noninvasive monitoring of blood glucose concentration in diabetic patients with optical coherence tomography. Laser Phys Lett. 2017;14:035603.
5. Miyachi Y, Hasegawa H, Kanai H. Automated detection of arterial wall boundaries based on correlation between adjacent receive scan lines for elasticity imaging. Jpn J Appl Phys. 2015;54:07HF18-1–-11.
6. Nagaoka R, Iwasaki R, Arakawa M, et al. Basic study of intrinsic elastography: relationship between tissue stiffness and propagation velocity of deformation induced by pulsatile flow. Jpn J Appl Phys. 2015;54:07HF08-1–8.
7. Sakai Y, Taki H, Kanai H. Accurate evaluation of viscoelasticity of radial artery wall during flow-mediated dilation in ultrasound measurement. Jpn J Appl Phys. 2016;55:07KF11-1–6.
8. Mochizuki Y, Taki H, Kanai H. Three-dimensional visualization of shear wave propagation generated by dual acoustic radiation pressure. Jpn J Appl Phys. 2016;55:07KF13-1–5.
9. Mori S, Ohashi M, Hirata S, et al. Stability evaluation of parameter estimation of multi-Rayleigh model for ultrasound B-mode image of liver fibrosis. Jpn J Appl Phys. 2016;55:07KF09-1–6.
10. Takahashi K, Taki H, Onishi E, et al. Imaging of human vertebral surface using ultrasound RF data received at each element of probe for thoracic anesthesia. Jpn J Appl Phys. 2017;56:07JF01-1–5.
11. Tobinai Y, Taki H, Kanai H. Mechanism of synchronized change in ultrasonic integrated backscatter across human heart wall. Jpn J Appl Phys. 2017;56:07JF04-1–6.
12. Matsuno Y, Taki H, Yamamoto H, et al. Ultrasound imaging of propagation of myocardial contraction for non-invasive identification of myocardial ischemia. Jpn J Appl Phys. 2017;56:07JF05-1–6.
13. Takahashi K, Taki H, Kanai H. Identification of the heart wall and chamber based on temporal change of ultrasonic scatterer distribution. Jpn J Appl Phys. 2017;56:07JF09-1–7.
14. Yoshida T, Sato K, Kondo T. Blood-mimicking fluid using glycols aqueous solution and their physical properties. Jpn J Appl Phys. 2014;53:07KF01-1–5.
15. Takahashi H, Hasegawa H, Kanai H. Echo speckle imaging of blood particles with high-frame-rate echocardiography. Jpn J Appl Phys. 2014;53:07KF08-1–7.
16. Paeng DG, Chiao RY, Shung KK. Echogenicity variations from porcine blood II: the "bright ring" under oscillatory flow. Ultrasound Med Biol. 2004;30:815–25.
17. Huang CC, Wang SH. Characterization of blood properties from coagulating blood of different hematocrits using ultrasonic backscatter and attenuation. Jpn J Appl Phys. 2006;45:7191–6.
18. Ikemoto S, Kuchiba K, Akiyama M, et al. Elevated viscoelasticity of blood in diabetic microangiopathy. J Jpn Diab Soc. 1988;31:231–7.
19. Paisey RB, Harkness J, Hartog M, et al. The effect of improvement in diabetic control on plasma and whole blood viscosity. Diabetologia. 1980;19:345–9.
20. Wang X, Liu L, Cheng T, et al. The relationship between intracardiovascular smoke-like echo and erythrocyte rouleaux formation. Am Heart J. 1992;124:961–5.
21. Libgot-Callé R, Ossant F, Gruel Y, et al. High frequency ultrasound device to investigate the acoustic properties of whole blood during coagulation. Ultrasound Med Biol. 2008;34:252–64.
22. Callé R, Plag C, Patat F, et al. Interest of the attenuation coefficient in multiparametric high frequency ultrasound investigation of whole blood coagulation process. J Acoust Soc Am. 2009;125:530–8.
23. Franceschini E, Yu F, Destrempes F, et al. Ultrasound characterization of red blood cell aggregation with intervening

attenuating tissue-mimicking phantoms. J Acoust Soc Am. 2010;127:1104–15.
24. Fukushima T, Hasegawa H, Kanai H. Estimation of scatterer diameter by normalized power spectrum of high-frequency ultrasonic RF echo for assessment of red blood cell aggregation. Jpn J Appl Phys. 2011;50:07HF02-1–8.
25. Kurokawa Y, Taki H, Yashiro S, et al. Estimation of size of red blood cell aggregates using backscattering property of high-frequency ultrasound: in vivo evaluation. Jpn J Appl Phys. 2016;55:07KF12-1–8.
26. Insana MF, Hall TJ. Parametric ultrasound imaging from backscatter coefficient measurements: image formation and interpretation. Ultrason Imaging. 1990;12:245–67.
27. Insana MF, Wagner RF, Brown DG, et al. Describing small-scale structure in random media using pulse-echo ultrasound. J Acoust Soc Am. 1990;87:179–92.
28. Fontaine I, Cloutier G. Modeling the frequency dependence (5–120 MHz) of ultrasound backscattering by red cell aggregates in shear flow at a normal hematocrit. J Acoust Soc Am. 2003;113:2893–900.
29. Morse PM, Feshbach H. Methods of theoretical physics. New York: McGrawHill; 1953.
30. Hashimoto Y, Akashi N, Kushibiki J. Measurements of ultrasonic attenuation coefficients of water in VHF/UHF range. Tech Rep IEICE. 1997;97:37–42.
31. Carstensen EL, Li K, Schwan HP. Determination of acoustic properties of blood and its components. J Acoust Soc Am. 1953;25:286–9.
32. Shiga T, Maeda N, Kon K. Erythrocyte rheology. Crit Rev Oncol Hematol. 1990;10:9–48.
33. World Health Organization & International Diabetes Federation. Definition and diagnosis of diabetes mellitus and intermediate hyperglycaemia: report of a WHO/IDF consultation. Geneva: World Health Organization; 2006. http://www.who.int/iris/handle/10665/43588. Accessed 20 Mar 2018.